JOURNAL OF SOLID STATE CHEMISTRY 16, 117–128 (1976)

$Ba_{15}Fe_7S_{25}$ and Ba_3FeS_5: Crystal Structures, Mössbauer, Magnetic, and Electrical Behavior

J. T. LEMLEY, J. M. JENKS, J. T. HOGGINS,
Z. ELIEZER, AND H. STEINFINK

Materials Science Laboratories, Department of Chemical Engineering, The University of Texas at Austin, Austin, Texas 78712

Received February 5, 1975; revised May 12, 1975

$Ba_{15}Fe_7S_{25}$ is prepared by reacting stoichiometric amounts of BaS, Fe, and S in evacuated quartz ampoules while Ba_3FeS_5 is obtained in a tetrahedral press at 50 kbars and 1000°C. The crystal structure of $Ba_{15}Fe_7S_{25}$ has been determined using 4053 independent, nonzero X-ray reflections measured by a counter technique. The compound crystallizes in the orthorhombic system, *Pnma*, $a = 41.91(1)$ Å, $b = 9.572(3)$ Å, $c = 12.654(3)$ Å, $\rho_{calc} = 4.26$ g/cm^3, $z = 4$; Ba_3FeS_5 also crystallizes in *Pnma*, $a = 12.405(1)$ Å, $b = 9.516(1)$ Å, $c = 8.5212(9)$ Å, $\rho_{calc} = 4.14$ g/cm^3, $z = 4$. In both compounds, Fe is tetrahedrally coordinated to S, and Ba is in either nine- or eight-fold coordination; a trigonal prism with three rectangular faces capped and a cube. Ba–S distances are about 3.4 Å, and Fe–S distances are 2.26 Å. In Ba_3FeS_5, single isolated tetrahedra are present. In $Ba_{15}Fe_7S_{25}$, eight isolated trinuclear units, formed by a central tetrahedron sharing one edge and one corner, respectively, with two terminal tetrahedra and four isolated single tetrahedra are present in the unit cell. The BaS_6 trigonal prisms form infinite columns by sharing the triangular faces. The columns share edges to form distorted hexagonal rings. Within the rings are additional S and Ba ions, and Fe in tetrahedral sites. The main difference between the two structures is the filling of the tetrahedral sites inside the hexagonal rings. The effective paramagnetic moment in $Ba_{15}Fe_7S_{25}$ is 5.5 μ_B, in good agreement with a value expected from $6Fe^{3+}$ and Fe^{2+} from the stoichiometry. The room temperature Mössbauer spectrum shows isomer shifts of 0.2 mm/sec. The data indicate that electron delocalization occurs across the edge-shared tetrahedra so that an effective charge distribution $5Fe^{3+}$ and $2Fe^{2.5+}$ is present. The material has a room temperature electrical resistivity of 10^5 ohm-cm. The effective magnetic moment for Ba_3FeS_5 is 5.1 μ_B as might be expected for Fe^{2+} or Fe^{4+}. One quadrupole split Mössbauer spectrum is observed with an isomer shift of 0.2 mm/sec, a value usually observed for Fe^{3+}. The observations are reconciled by postulating the delocalization of an electron within the tetrahedral configuration. The room temperature electrical resistivity is 10^5 ohm-cm.

Introduction

The investigation of the barium–iron–sulfur system has revealed a large number of compounds with complex stoichiometries in which the oxidation state of iron within a given compound may consist of divalent, trivalent, or mixed valence states (*1*, *2*). Thus, it is possible that the various valence states of iron may be localized in definite crystallographic sites, or the different valence states may be distributed randomly over crystallographic sites, or the electrons may be delocalized. By means of Mössbauer spectroscopy, and magnetic and electrical resistivity measurements we have recently shown (*2*) that all of these possibilities are found among the compounds synthesized and investigated in the Ba–Fe–S system. In a continuing investigation, we have synthesized and characterized two additional phases, $Ba_{15}Fe_7S_{25}$ and Ba_3FeS_5. On the basis of electrical neutrality requirements and on the assumption that only S^{2-} ions are present in the structures, the former compound must have one divalent and six trivalent irons while the latter compound

must contain only tetravalent iron. We report here the structural determination as well as results of the Mössbauer, magnetic and electrical measurements that permit us to reach a conclusion concerning the oxidation state of iron in these two compounds and that are consistent with previous observations in related phases (*2*).

Experimental

$Ba_{15}Fe_7S_{25}$ was prepared by reacting stoichiometric amounts of BaS, Fe, and S in sealed evacuated quartz ampoules at 800°C for 2 days. Black single crystals of this compound were selected from the reaction product and used in the structural investigation. Ba_3FeS_5 was synthesized in a tetrahedral press at about 50 kbars and 1000°C. Single crystals were selected from the reaction product and used in the further investigations.

Mössbauer spectra were obtained using a constant acceleration drive operated in the time mode. Data were accumulated in a 400-channel analyzer. The source was 20 mCi of Co^{57} diffused into copper foil and used at room temperature. Velocity calibration was obtained using a laser interferometer (*3*). The absorbers consisted of finely ground powder approximately 150 mg/in.^{2} thick. The spectra were fitted by least-squares analysis assuming Lorentzian line shapes and using a modified National Bureau of Standards program. The reproducibility for values of isomer shifts is $\pm$ 0.02 mm/sec.

Electrical resistivity measurements were carried out on pressed and sintered samples produced by applying a pressure of about 10 000 psi to a finely powdered specimen and then heating it under vacuum at 400°C for about 2 days. A conventional four probe method was used for the rectangular pressed samples with high temperature measurements being made in a protective atmosphere of argon.

The measurements of magnetic susceptibility as a function of temperature were carried out on a Faraday balance with the susceptibility calibration being done using $Hg[Co(CNS)_4]$ as a calibrant. The possible influence of ferromagnetic impurities on the susceptibility data was eliminated by the method of Honda and Owen (*4*).

$Ba_{15}Fe_7S_{25}$

Weissenberg and Buerger precession photographs obtained from a single crystal showed that the diffraction symmetry was *mmm*, with systematic absences $0kl$, $k + l = 2n + 1$ and $hk0$, $h = 2n + 1$ consistent with space groups $Pn2_1a$ and *Pnma*. Lattice constants were determined from a least-squares refinement of precise 2θ measurements of 30 reflections between 30° and 50° from a crystal mounted on a single-crystal diffractometer with the instrument set at a 1° take-off angle and a 0.05° slit in front of the scintillation counter and using Mo radiation $\lambda_1 = 0.70926$ Å and $\lambda_2 = 0.71354$ Å. The lattice constants at room temperature were $a = 41.91(1)$ Å, $b = 9.572(3)$ Å, $c = 12.654(3)$ Å; $\rho_{calc} = 4.26$ g/cm^3, $z = 4$. A crystal approximately $0.10 \times 0.072 \times 0.13$ mm was selected for three-dimensional *X*-ray intensity data collection with a linear diffractometer using the stationary counter-moving crystal technique, and Mo$K\alpha_1$ radiation monochromatized by a graphite single crystal. The crystal was aligned so that the spindle axis of the machine was parallel to the *b*-axis. For each reflection, the intensity was integrated by rotating ω at the rate of 1°/min. The interval of integration ranged from 1.2° to 2.4° for reflections having $\Upsilon > 40°$ and from 1.6° to 2.8° for those having $\Upsilon \leqslant 40°$. Background intensities were counted at both ends of the interval of integration for 12 sec. When the integrated intensity was less than 400 counts the same ω scan was repeated once more. The intensities were measured using a circular receiving aperture 1° wide in front of the scintillation counter. The channel width of the pulse height analyzer was set to accept 85% of the incident power. Twelve reciprocal lattice layers were explored out to $(\sin\theta)/\lambda = 0.65$ with 5489 independent reflections being measured. The intensities were transformed into structure factor amplitudes through the application of Lorentz and polarization corrections. No absorption correction was applied because the irregular shape of the crystal made an accurate description impossible ($\mu_l = 147.05$ cm^{-1}). The basis for accepting a

reflection as statistically non zero was $\Delta I/I < 0.5$, where $\Delta I/I = (T + t^2B)^{1/2}/(T - tB)$ with T = total counts in time t_T for the ω scan, B = total background counts, $t = t_T/(t_1 + t_2)$ where t_1 and t_2 are background counting times and, in this case, were equal. Of the 5489 independent reflections, 4053 satisfied this criterion. The standard deviations for the structure factor amplitudes were estimated by the formula

$$\sigma(F) = \left\{\left(\frac{F}{2I}\right)^2\left[I + \frac{Bt}{2} + 0.0004(I^2)\right]\right\}^{1/2}$$

and $1/\sigma^2$ was used as weights in the least-squares calculations.

Ba_3FeS_5

Weissenberg and Buerger precession photographs were taken of a crystal selected from the reaction product. The compound showed diffraction symmetry *mmm* with systematic absences $0kl$, $k + l = 2n + 1$ and $hk0$, $h = 2n + 1$ consistent with space groups $Pn2_1a$ and *Pnma*.

Lattice constants were obtained by mounting the crystal on a quarter circle diffractometer and using Mo$K\alpha$ radiation ($\lambda_1 = 0.70926$ Å, $\lambda_2 = 0.71354$ Å), with the instrument set at a take off angle of 1° and a 0.05° slit in front of the aperture of the scintillation counter. Forty measurements of 2θ between the values of 30° to 45° were made and a least-squares fit of the data yielded $a = 12.405(1)$ Å, $b = 9.516(1)$ Å, $c = 8.5212(9)$ Å; $\rho_{calc} = 4.14$ g/cm^3, $z = 4$.

Three dimensional *X*-ray diffraction intensity data to $(\sin\theta)/\lambda = 0.65$ were collected with Mo$K\alpha$ radiation using a stationary crystal-stationary counter technique, balanced filters, a 5° take-off angle, no slit in front of the counter window, and the channel width of the pulse height analyser set to accept 85% of the incident energy. The mosaic spread of the crystal, evaluated from an ω scan, was < 0.4° measured at the base of the peaks. Intensities were counted for 10 sec with a Zr filter and then background was measured for 10 sec with a Y filter. A total of 1237 independent reflections was measured and 845 reflections were considered observed on the basis that the peak count exceeded the background count by six counts. The measured intensities were transformed into a set of structure amplitudes after Lorentz, polarization, and absorption corrections were applied. The crystal, approximately 0.10 × 0.13 × 0.06 mm, was described by six planes and the transmission factor varied between 0.312 and 0.513 (μ_l = 143.5 cm^{-1}). The standard deviation of the structure factor was estimated from the equation

$$\sigma(F) = \frac{1}{2}\left(K\frac{1+b}{1-b}\right)^{1/2},$$

where $b = I_Y/I_{Zr}$ is the background to peak ratio and K is the product of the absorption, Lorentz, and polarization corrections.

Structure Determination

The direct method for determination of phases was used in the solution of the structure of $Ba_{15}Fe_7S_{25}$. A Wilson plot was constructed to provide an approximate scale factor and to indicate a centric distribution of intensities, indicating the space group to be *Pnma*. The computer programs FAME (by R. B. K. Dewar) and MULTAN (by P. Main, M. Woolfson, and G. Germain) were used to generate 440 phases from four symbol assigned reflections. An E-map based on the solution with the highest figure of merit (ABS FOM) revealed the positions of eight barium and two iron atoms. A Fourier map based on these 10 atomic positions gave the positions of the remaining 27 atoms. The structure was refined by a least-squares procedure using a modification of the program ORFLS (by W. R. Busing, H. A. Levy, and K. O. Martin). The quantity minimized was $\sum w(KF_o - F_c)^2$ with weights w equal to $1/\sigma^2$. The atomic scattering factors for Ba, Fe, and S are those published in (*5*) and were corrected for the real part of dispersion effects. Table I contains the final atomic parameters obtained from a least-squares refinement based on 4053 reflections greater than 2σ. The discrepancy indices for the final structure factors are as follows: For all observed reflections $R = 0.072$, $wR = 0.079$ $(R = \sum ||F_o| - |F_c||/\sum |F_o|$, $wR = [\sum w(F_o - F_c)^2/\sum wF_o^2]^{1/2})$. The

TABLE I

FINAL ATOMIC PARAMETERS AND THEIR STANDARD DEVIATIONS (× 10^4) IN PARENTHESES FOR $Ba_{15}Fe_7S_{25}$[a]

Atom	X	Y	Z	β_{11}	β_{22}	β_{33}	β_{12}	β_{13}	β_{23}
Ba1	149(0)	5267(1)	1577(1)	2(0)	37(2)	25(1)	−1(0)	−1(0)	−1(1)
Ba2	240(0)	3/4	4543(2)	2(0)	35(3)	20(1)	0	0(0)	0
Ba3	1084(0)	4886(1)	3432(1)	2(0)	47(2)	24(1)	0(0)	1(0)	1(1)
Ba4	1124(0)	3/4	5920(1)	2(0)	33(3)	19(1)	0	1(0)	0
Ba5	2253(0)	3/4	4976(2)	2(0)	35(3)	28(1)	0	1(0)	0
Ba6	3156(0)	5274(1)	3951(1)	3(0)	50(2)	30(1)	−0(0)	1(0)	−0(1)
Ba7	3153(0)	3/4	807(2)	4(0)	36(3)	25(1)	0	2(0)	0
Ba8	4066(0)	4958(1)	2042(1)	3(0)	50(3)	23(1)	−0(0)	−1(0)	−1(1)
Ba9	4139(0)	3/4	4840(2)	2(0)	36(3)	21(1)	0	−1(0)	0
Ba10	2147(0)	5156(2)	2215(2)	4(0)	70(3)	66(1)	2(0)	−6(0)	−40(1)
Fe1	299(1)	1/4	3396(4)	2(0)	38(5)	10(3)	0	−0(1)	0
Fe2	1451(1)	3/4	5096(4)	1(0)	40(5)	13(3)	0	−1(1)	0
Fe3	1589(1)	1/4	1532(4)	2(0)	20(4)	11(3)	0	−0(1)	0
Fe4	2650(1)	1/4	4428(4)	2(0)	60(6)	31(4)	0	1(1)	0
Fe5	3293(1)	1/4	2050(4)	1(0)	37(5)	11(3)	0	−1(1)	0
Fe6	4435(1)	3/4	3940(4)	1(0)	37(5)	13(3)	0	0(1)	0
Fe7	4635(1)	1/4	3976(4)	1(0)	23(4)	10(3)	0	1(1)	0
S1	88(2)	1/4	71(6)	2(0)	49(8)	14(5)	0	0(1)	0
S2	373(2)	4381(6)	4465(5)	3(0)	46(6)	36(4)	1(1)	0(1)	0(4)
S3	635(2)	3/4	2440(7)	3(0)	40(7)	18(5)	0	0(1)	0
S4	668(2)	1/4	2176(7)	2(0)	97(10)	19(5)	0	0(1)	0
S5	1362(2)	4518(5)	1061(5)	4(0)	34(6)	21(4)	2(1)	1(1)	−0(4)
S6	1686(3)	1/4	3266(8)	5(1)	66(9)	29(6)	0	−3(2)	0
S7	1635(2)	3/4	3400(7)	2(0)	52(8)	22(6)	0	0(1)	0
S8	1904(2)	3/4	506(8)	2(0)	51(8)	54(8)	0	−3(2)	0
S9	2058(2)	1/4	686(7)	1(0)	43(8)	41(7)	0	0(1)	0
S10	2398(1)	4453(5)	4772(5)	2(0)	38(5)	41(5)	3(1)	2(1)	−0(4)
S11	2781(1)	1/4	2628(8)	3(0)	130(12)	22(6)	0	3(2)	0
S12	3354(1)	4397(6)	1001(5)	2(0)	48(6)	33(4)	0(1)	−1(1)	−3(4)
S13	3637(2)	3/4	3036(7)	2(0)	45(8)	27(6)	0	2(1)	0
S14	3661(2)	1/4	3274(7)	3(0)	55(8)	21(6)	0	−3(1)	0
S15	3907(2)	3/4	289(7)	0(0)	53(8)	43(6)	0	−1(1)	0
S16	4071(2)	1/4	271(7)	2(0)	54(8)	30(6)	0	2(1)	0
S17	4390(1)	4510(5)	4352(5)	3(0)	36(5)	27(4)	1(1)	0(1)	0(4)
S18	4633(2)	3/4	2089(7)	3(0)	75(10)	25(6)	0	−0(1)	0
S19	4776(2)	1/4	2210(7)	4(1)	89(10)	17(5)	0	−0(2)	0
S20	2656(2)	3/4	2765(8)	2(0)	35(7)	57(7)	0	6(2)	0

[a] The temperature factor is $\exp[-(\beta_{11}h^2 + \beta_{22}k^2 + \beta_{33}l^2 + 2\beta_{12}hk + 2\beta_{13}hl + 2\beta_{23}kl)]$.

observed and calculated structure amplitudes are available.[1] For all reflections the final R was 0.108. A difference electron density map calculated with the last set of parameters gave no physically significant peaks.

The structure for Ba_3FeS_5 was solved from an interpretation of the three-dimensional Patterson function, which yielded the position of one barium. A three-dimensional electron density map phased on the barium atom yielded the positions of the other six atoms. The structure was refined by least squares, as

[1] "See NAPS Document No. 02595 for 31 pages of supplementary material. Order from ASIS/NAPS c/o Microfiche Publications, 440 Park Avenue South, New York, N.Y. 10016. Remit in advance for each NAPS accession number. Make checks payable to Microfiche Publications." Photocopies are $5.15. Microfiche are $1.50. Outside of the United States and Canada, postage is $2.00 for a photocopy or $0.50 for a fiche.

TABLE II

FINAL ATOMIC PARAMETERS AND THEIR STANDARD DEVIATIONS ($\times 10^4$) IN PARENTHESES FOR Ba_3FeS_5[a]

Atom	X	Y	Z	β_{11}	β_{22}	β_{33}	β_{12}	β_{13}	β_{23}
Ba1	1666(1)	197(1)	946(2)	25(1)	41(1)	62(2)	−4(1)	−2(1)	−2(2)
Ba2	4823(1)	3/4	774(2)	27(1)	33(2)	47(2)	0	−4(2)	0
Fe	1055(3)	3/4	8157(5)	12(3)	35(5)	30(6)	0	−3(3)	0
S1	2839(6)	3/4	8278(9)	19(5)	57(9)	54(11)	0	−9(6)	0
S2	4282(4)	4508(6)	1914(6)	26(3)	40(6)	62(8)	1(4)	2(4)	2(6)
S3	77(6)	3/4	389(8)	16(4)	49(9)	32(10)	0	6(6)	0
S4	2280(6)	3/4	3402(11)	12(5)	59(10)	102(14)	0	−3(7)	0

[a] The temperature factor is $[\exp -(\beta_{11}h^2 + \beta_{22}k^2 + \beta_{33}l^2 + 2\beta_{12}hk + 2\beta_{13}hl + 2\beta_{23}kl)]$.

described previously. For all observed reflections the final $R = 0.051$, $wR = 0.055$, and the atomic parameters are shown in Table II. For all reflections the final R was 0.102. A difference electron density map calculated with the last set of parameters showed no peak greater than 1.0e $Å^{-3}$.

Discussion of the Structures

A stereoscopic drawing of $Ba_{15}Fe_7S_{25}$ is shown in Fig. 1 and the important interatomic distances and angles are tabulated in Table III. Fig. 2 shows a drawing of Ba_3FeS_5 and the interatomic distances and angles are listed in Table IV. In both compounds, Fe is tetrahedrally coordinated to S while Ba is in eight- or ninefold coordination with S making a distorted cubic prism and a trigonal prism with the three rectangular faces capped. In the 3–1–5 structure single isolated tetrahedra are present. In 15–7–25, two isolated trinuclear units shown in Fig. 3 and an isolated single tetrahedron containing Fe3 are present in the asymmetric unit. The trinuclear units have a central tetrahedron sharing one corner and one edge, respectively, with the two terminal tetrahedra. The Ba–S distances are about 3.4 Å and Fe–S distances are about 2.26 Å in both compounds.

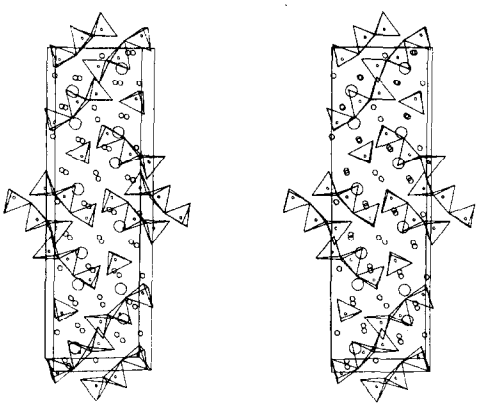

FIG. 1. Stereoscopic view of the structure of $Ba_{15}Fe_7S_{25}$. The a-axis is vertical and the c-axis horizontal. S atoms are located at the corners of the tetrahedra and the small circles within the tetrahedra are Fe; large circles are S not bonded to Fe; smaller circles are Ba.

The trinuclear unit in 15–7–25 is not part of an infinite chain. This is unlike the case of $Ba_7Fe_6S_{14}$ (*6*) in which trinuclear units, comprised of a central tetrahedron sharing opposite edges with terminal tetrahedra, are interconnected by corner sharing into infinite chains. The mean Fe–S distances for each tetrahedron are:

$\langle Fe1\text{–}S\rangle = 2.264$ $\langle Fe2\text{–}S\rangle = 2.268$ $\langle Fe3\text{–}S\rangle = 2.235$
$\langle Fe4\text{–}S\rangle = 2.260$ $\langle Fe5\text{–}S\rangle = 2.246$ $\langle Fe6\text{–}S\rangle = 2.278$
$\langle Fe7\text{–}S\rangle = 2.258$

On the basis of stoichiometry one Fe^{2+} and six Fe^{3+} should be present in the formula unit. The four Fe3–S distances are approximately equal and the average distance agrees very well with that observed in $KFeS_2$ (*7*). We suggest that this site contains only Fe^{3+}.

TABLE III

BOND DISTANCES AND ANGLES IN $Ba_{15}Fe_7S_{25}$

Distances (Å)

Ba1–S1	3.274(4)	Ba6–S5	3.354(6)	2Fe1–S2	2.274(7)
Ba1–S1	3.148(4)	Ba6–S8	3.316(4)	Fe1–S4	2.186(10)
Ba1–S2	3.867(7)	Ba6–S9	3.189(4)	Fe1–S19	2.323(11)
Ba1–S3	3.147(4)	Ba6–S10	3.435(6)	S2–S2	3.602(8)
Ba1–S4	3.510(4)	Ba6–S11	3.512(4)	2S2–S4	3.628(8)
Ba1–S17	3.471(6)	Ba6–S12	3.916(6)	2S2–S19	3.742(8)
Ba1–S17	3.422(6)	Ba6–S13	3.152(4)	S4–S19	3.819(13)
Ba1–S18	3.480(5)	Ba6–S14	3.503(4)		
Ba1–S19	3.439(4)	Ba6–S20	3.347(4)	Fe2–S7	2.281(10)
				2Fe2–S12	2.297(7)
2Ba2–S2	3.040(6)	Ba7–S6	3.288(10)	Fe2–S16	2.199(9)
2Ba2–S2	3.379(6)	2Ba7–S10	3.246(6)	2S7–S12	3.759(8)
Ba2–S3	3.134(9)	2Ba7–S12	3.099(6)	S7–S16	3.792(12)
Ba2–S16	3.032(8)	Ba7–S13	3.475(9)	S12–S12	3.632(8)
Ba2–S18	3.278(9)	Ba7–S15	3.231(7)	2S12–S16	3.630(8)
Ba2–S19	3.376(9)	Ba7–S20	3.236(9)		
				2Fe3–S5	2.234(6)
Ba3–S2	3.291(6)	Ba8–S2	4.070(7)	Fe3–S6	2.232(11)
Ba3–S3	3.374(4)	Ba8–S12	3.306(6)	Fe3–S9	2.239(9)
Ba3–S4	3.285(4)	Ba8–S13	3.279(4)	S5–S5	3.766(8)
Ba3–S5	3.238(6)	Ba8–S14	3.294(4)	2S5–S6	3.655(8)
Ba3–S6	3.409(4)	Ba8–S15	3.360(4)	2S5–S9	3.531(7)
Ba3–S7	3.407(4)	Ba8–S16	3.250(4)	S6–S9	3.618(13)
Ba3–S12	4.072(6)	Ba8–S17	3.251(6)		
Ba3–S15	3.279(4)	Ba8–S18	3.400(4)	Fe4–S8	2.313(11)
Ba3–S16	3.479(4)	Ba8–S19	3.799(5)	2Fe4–S10	2.191(6)
				Fe4–S11	2.344(11)
Ba4–S3	3.111(9)	Ba9–S1	3.254(8)	2S8–S10	3.592(7)
2Ba4–S5	3.082(6)	Ba9–S4	3.066(9)	S8–S11	3.874(14)
Ba4–S7	4.151(9)	2Ba9–S5	3.244(6)	S10–S10	3.739(7)
Ba4–S8	3.273(9)	Ba9–S13	3.104(9)	2S10–S11	3.665(8)
Ba4–S14	3.068(9)	2Ba9–S17	3.112(6)		
Ba4–2S17	3.286(6)	Ba9–S18	4.050(9)	Fe5–S11	2.268(10)
				2Fe5–S12	2.264(7)
Ba5–S7	3.268(9)	Ba10–S5	3.652(6)	Fe5–S14	2.188(10)
Ba5–S9	3.024(8)	Ba10–S6	3.460(4)	2S11–S12	3.649(8)
2Ba5–S10	2.991(6)	Ba10–S7	3.447(4)	S11–S14	3.780(13)
Ba5–S11	3.360(10)	Ba10–S8	3.279(4)	S12–S12	3.632(8)
2Ba5–S12	3.386(6)	Ba10–S9	3.217(4)	2S12–S14	3.638(8)
Ba5–S20	3.267(9)	Ba10–S10	3.469(7)		
		Ba10–S10	3.652(7)	2Fe6–S2	2.297(7)
		Ba10–S11	3.715(4)	Fe6–S15	2.215(8)
		Ba10–S20	3.173(4)	Fe6–S18	2.301(10)
				S2–S2	3.602(8)
				2S2–S15	3.665(8)
				2S2–S18	3.779(8)
				S15–S18	3.779(12)

TABLE III (*continued*)

Distances (Å)					
		Some nonbonded Fe–Fe distances			
Fe7–S1	2.250(9)			Fe3–Fe4	5.763(7)
2Fe7–S17	2.234(6)			Fe3–Fe4	6.339(5)
Fe7–S19	2.312(10)	Fe1–Fe1	6.759(5)	Fe3–Fe5	7.173(7)
2S1–S17	3.580(7)	Fe1–Fe2	7.131(5)	Fe3–Fe5	7.438(5)
S1–S19	3.682(12)	Fe1–Fe2	7.579(7)	Fe3–Fe6	6.503(7)
S17–S17	3.849(7)	Fe1–Fe3	5.898(7)	Fe3–Fe7	7.725(5)
2S17–S19	3.698(8)	Fe1–Fe6	6.195(5)	Fe4–Fe5	7.038(5)
		Fe1–Fe7	7.367(5)	Fe5–Fe6	7.086(5)
Fe1–Fe6	2.764(7)	Fe2–Fe3	6.602(5)	Fe5–Fe7	6.131(6)
Fe1–Fe7	4.094(6)	Fe2–Fe4	6.991(5)	Fe6–Fe6	6.809(5)
Fe2–Fe5	2.696(7)	Fe2–Fe4	6.653(7)	Fe6–Fe7	6.646(5)
Fe4–Fe5	4.040(7)	Fe2–Fe6	6.069(5)	Fe6–Fe7	6.767(6)
		Fe2–Fe7	6.696(6)	Fe7–Fe7	6.244(5)

Angles (degrees)			
S2–Fe1–S2	104.8(3)	S11–Fe5–S12	107.3(2)
S2–Fe1–S4	108.9(2)	S11–Fe5–S14	116.1(4)
S2–Fe1–S19	109.0(2)	S12–Fe5–S12	106.7(3)
S4–Fe1–S19	115.8(4)	S12–Fe5–S14	109.6(2)
S7–Fe2–S12	110.4(2)	S2–Fe6–S2	103.3(3)
S7–Fe2–S16	115.6(4)	S2–Fe6–S15	108.6(2)
S12–Fe2–S12	104.5(3)	S2–Fe6–S18	110.6(2)
S12–Fe2–S16	107.7(2)	S15–Fe6–S18	114.6(4)
S5–Fe3–S5	119.7(3)	S1–Fe7–S17	105.9(2)
S5–Fe3–S6	109.9(2)	S1–Fe7–S19	107.6(4)
S5–Fe3–S9	104.2(2)	S17–Fe7–S17	119.0(3)
S6–Fe3–S9	108.1(4)	S17–Fe7–S19	108.9(2)
S8–Fe4–S10	105.8(2)	Fe6–Fe1–Fe7	161.0(2)
S8–Fe4–S11	112.6(4)	Fe2–Fe5–Fe4	161.6(2)
S10–Fe4–S10	117.2(3)		
S10–Fe4–S11	107.8(2)		

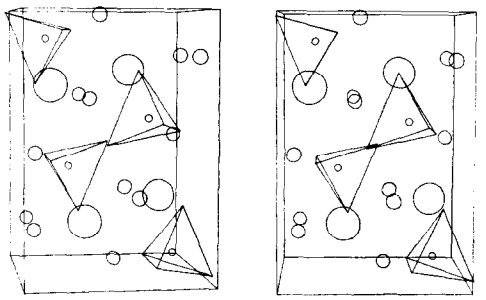

FIG. 2. Stereoscopic view of the structure of Ba_3FeS_5. The *a*-axis is vertical and *c* is the horizontal axis. The atom designations are the same as for Fig. 1.

If a site were occupied exclusively by a Fe^{2+} ion, then the Fe–S distances within this tetrahedron should be approximately 2.37 Å (*8*). This is not seen in this structure; therefore, either the distribution is random, or there is a delocalization of the electrons, or both. Electron delocalization would be expected between Fe in edge-sharing tetrahedra since this distance is about 2.7 Å (Fig. 3). Thus, if Fe^{2+} is located only in the terminal tetrahedron joined by corner sharing, there should be a lengthening of the Fe–S distances. Actually the average Fe–S distances are within about two standard deviations and no definitive

TABLE IV

BOND DISTANCES AND ANGLES IN Ba_3FeS_5

Distances (Å)					
Ba1–S1	3.287(2)	Ba2–S1	3.017(8)	2S1–S2	3.601(6)
Ba1–S1	3.504(2)	2Ba2–S2	3.083(6)	S1–S3	3.709(8)
Ba1–S2	3.486(5)	2Ba2–S2	3.183(6)	S2–S2	3.822(8)
Ba1–S2	3.361(5)	Ba2–S3	3.285(2)	S2–S3	3.613(6)
Bal–S2	3.691(6)	Ba2–S4	3.869(8)		
Ba1–S3	3.283(2)	Ba2–S4	3.128(8)	Some Non-bonded	
Ba1–S3	3.271(2)			Fe–Fe Distances	
Ba1–S4	3.399(2)	Fe–S1	2.266(9)	Fe–Fe	7.324(3)
Ba1–S4	3.349(2)	2Fe–S2	2.225(6)	Fe–Fe	7.645(3)
		Fe–S3	2.256(4)	Fe–Fe	6.274(2)
				Fe–Fe	6.303(5)

Angles (degrees)			
S1–Fe–S2	106.6(2)	S2–Fe–S2	118.4(3)
S1–Fe–S3	110.1(3)	S2–Fe–S3	107.5(2)

conclusion concerning the type of disorder is possible.

The characteristics of the inverse magnetic susceptibility versus temperature for $Ba_{15}Fe_7S_{25}$ are shown in Fig. 4. An effective moment of 5.5 μ_B was obtained from a fit to the linear portion of the susceptibility curve, in good agreement with the average spin only magnetic moment of 5.77 μ_B expected from six trivalent and one divalent iron atoms.

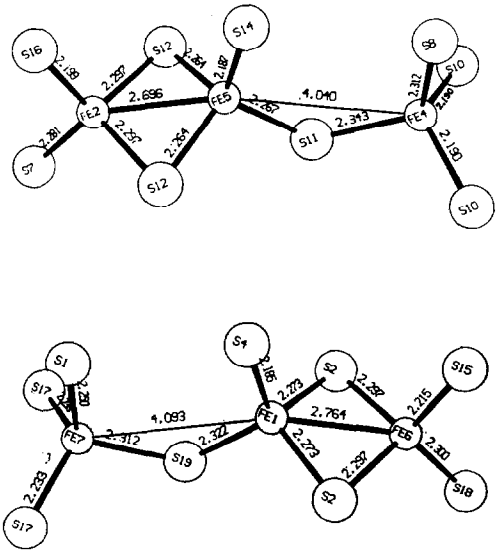

FIG. 3. The two trinuclear units, Fe_3S_9, in the structure of $Ba_{15}Fe_7S_{25}$. The slight discrepancies between distances shown and those given in Table III are due to computer round-off errors. The thin line represents a nonbonding distance.

The Mössbauer spectra show quadrupole split lines (Fig. 5). A least-squares fit to each of the spectra using two Lorentzians gave isomer shifts of 0.20 mm/sec at 300°K and 0.31 mm/sec at 78°K, and quadrupole splittings of 0.91 and 0.85 mm/sec, respectively. These values are relative to α-Fe and are consistent with those for Fe^{3+} observed in other compounds of the Ba–Fe–S system (*2*). These spectra are composed of seven overlapping quadrupole split doublets corresponding to the seven crystallographically independent iron atoms. The relatively broad peaks are caused by slightly different quadrupole splitting at each site. The Fe^{2+} ion is characterized by an isomer shift of 0.6 mm/sec and quadrupole splitting of approximately 2.5 mm/sec (*2*) at room temperature. This set of lines does not appear to be present in the spectrum. One possible reason for this is that the Fe^{2+} ion is on one of the edge-sharing tetrahedral sites and that delocalization of the electron across the shared edge has in effect produced a charge distribution of $5Fe^{3+}$ and $2Fe^{2.5+}$. This then occurs randomly at each of the two edge-shared units. A theoretical curve based on this

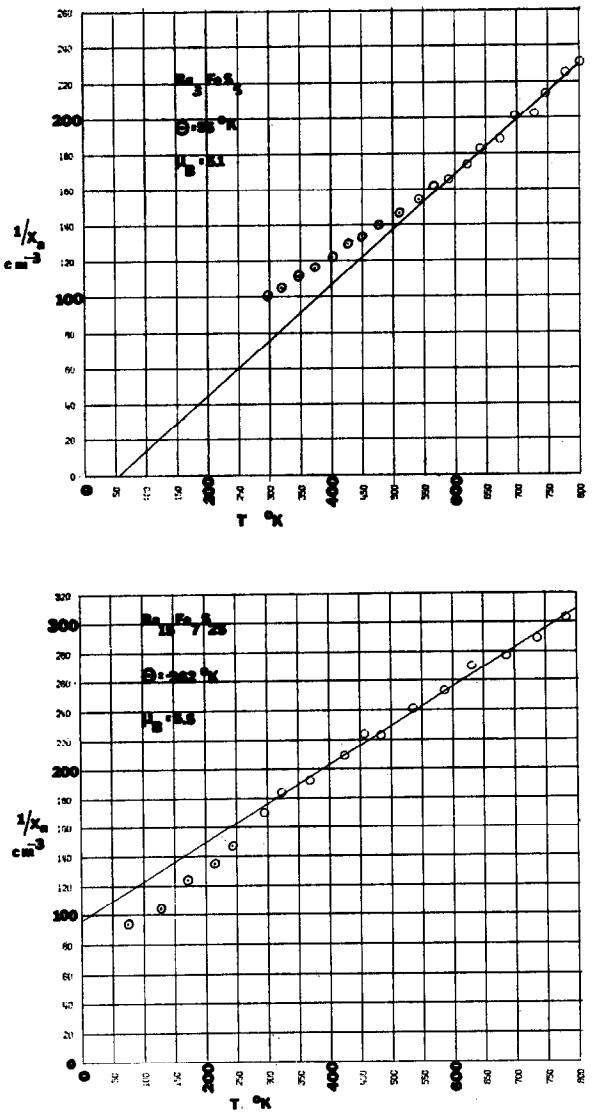

FIG. 4. Inverse magnetic susceptibility versus T for Ba_3FeS_5 and $Ba_{15}Fe_7S_{25}$.

mixture was calculated and is consistent with the observed spectrum.

On the basis of the Mössbauer results this material can be expected to exhibit a high value of the electrical resistivity, comparable to that observed in $Ba_7Fe_6S_{14}$. A small single-phase chunk was selected from the reaction product and the resistivity versus $1/T$ measurements (Fig. 6) indicate that it is a high resistivity semiconductor.

The inverse magnetic susceptibility versus temperature behavior of Ba_3FeS_5 is shown in Fig. 4. The effective moment obtained from a fit to the linear portion of the curve is 5.1 μ_B, corresponding closely to the value expected for Fe^{2+} or Fe^{4+}. The isomer shifts obtained from Mössbauer spectra at 300 and 78°K are 0.17 and 0.26 mm/sec, respectively. At both temperatures, only one quadrupole splitting is observed, that of 0.50 mm/sec. The value of

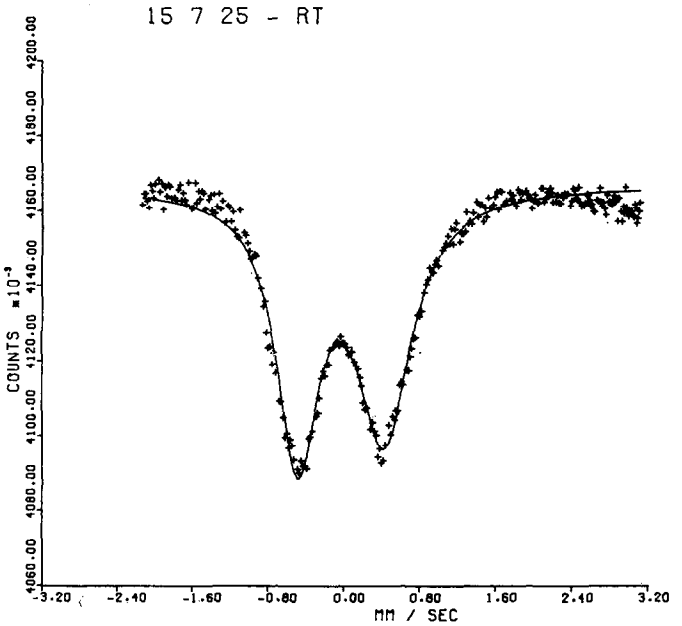

FIG. 5. Observed Mössbauer spectrum of $Ba_{15}Fe_7S_{25}$ and a calculated one fitted by least squares.

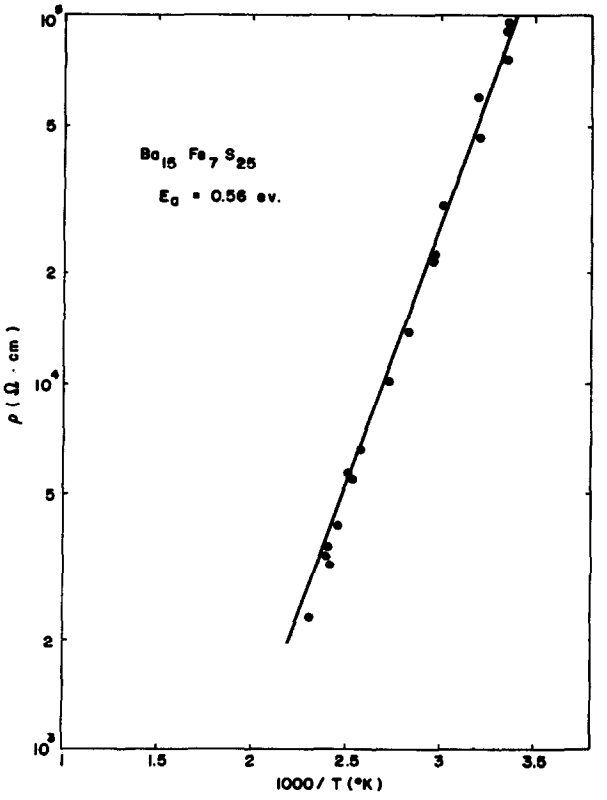

FIG. 6. Electrical resistivity versus $1/T$ for $Ba_{15}Fe_7S_{25}$.

the isomer shift is consistent with Fe^{3+}on the basis of our previous investigation on other compounds in the Ba–Fe–S system (*2*). The apparent disagreement between the observed magnetic moment, consistent with either Fe^{2+} or Fe^{4+}, and the Mössbauer isomer shift, consistent with Fe^{3+}, can be resolved by the supposition that back donation of electrons occurs. It becomes difficult to define a precise value of the oxidation state of Fe within the tetrahedron if this back donated electron density is delocalized. This density would not contribute significantly to the measured paramagnetic moment but would cause the isomer shift to resemble that for Fe^{3+} (*9*). The electrical resistivity of this material is predicted to be fairly high because the FeS_4 units are isolated. Indeed a room temperature measurement on a minute chunk yields a value of about 10^5 ohm-cm.

The description of the structure in terms of articulations of tetrahedra is very useful for an understanding of the physical behavior of the materials. However, the crystal chemical relationship between these two structures, as well as with previously published structures, becomes more evident when the description is based on the articulation of BaS_6 trigonal prisms (*10*, *11*). Fig. 7 shows the [010] and [0$\bar{1}$0] projections of $Ba_{15}Fe_7S_{25}$ and Ba_3FeS_5, respectively. Columns of trigonal prisms formed by sharing the two triangular faces are fused into distorted hexagonal rings by edge-sharing. This arrangement of prisms is quite similar to that found in Rh_5Ge_3 and β-Yb_5Sb_3 (*12*, *13*). Indeed the lattice constants for the latter are nearly identical to those for Ba_3FeS_5. The main differences among these four structures are due to the filling of space within the hexagonal rings.

The adjacent projections in Fig. 7 of five unit cells of Ba_3FeS_5 ($Ba_{15}Fe_5S_{25}$) and one unit cell of $Ba_{15}Fe_7S_{25}$ serve to accentuate the similarities between the two structures and at the same time to point out the differences. The configurations of atoms within the hexagonal rings are very similar. The coordination polyhedra about the barium atoms inside the rings are distorted cubes. They share opposite edges, but are displaced along the edges to

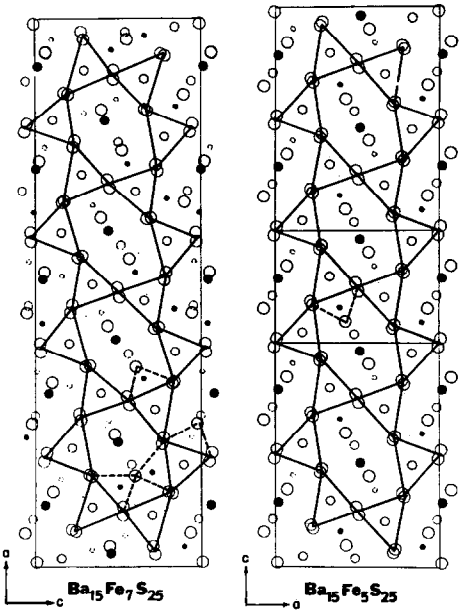

FIG. 7. The [010] and [0$\bar{1}$0] projections of the unit cell of $Ba_{15}Fe_7S_{25}$ and of five unit cells of Ba_3FeS_5. The large circles are S, the smaller circles are Ba, and the smallest are Fe. S at the corners of the prisms are at $y = \frac{1}{4}, \frac{3}{4}$; Ba in the prisms are at $y = 0, \frac{1}{2}$. Within the hexagonal rings, Ba and Fe at $y = \frac{3}{4}$ above the plane are indicated by solid circles, while those at $y = \frac{1}{4}$ are open, and the S atoms are at $y \approx 0, \frac{1}{2}$. The dashed lines outline one trinuclear tetrahedral unit in $Ba_{15}Fe_7S_{25}$ and an isolated tetrahedron in each structure.

form a corrugated one-dimensional array with its axis parallel to the axis of the columns formed by the prisms. One of the major differences between the two structures is the filling by Fe atoms of the tetrahedral holes produced between these two frameworks. The structure of Ba_3FeS_5 (Fig. 7) has two unoccupied tetrahedral sites on each side of the occupied site, i.e., three tetrahedra are formed in which the central one shares two faces. In some of the rings in $Ba_{15}Fe_7S_{25}$, the two outside tetrahedra are now occupied instead. Of the 10 rings in the unit cell of $Ba_{15}Fe_7S_{25}$, four contain only two Fe atoms, as in Ba_3FeS_5, four contain three Fe atoms, and two contain four Fe atoms. As a result, the chemical content of the equivalently sized unit cells changes from $Ba_{15}Fe_5S_{25}$ for the high pressure phase to $Ba_{15}Fe_7S_{25}$ for the

ambient pressure phase. The other major difference between the two structures is in the articulations of the bariums inside the rings. In $Ba_{15}Fe_7S_{25}$ the articulation is the same in all rings, but in Ba_3FeS_5 the articulation is reversed between adjacent rows of rings.

The examination of the structures using BaS_6 prisms brings out their close relationship and indeed explains why attempts to react a mixture of 3BaS:Fe:2S at ambient pressure always yields the phase $Ba_{15}Fe_7S_{25}$. The apparent anomaly in the density, in which the high pressure phase has a lower density than the ambient pressure phase, is also resolved because on the basis of equivalent mass content, i.e., $Ba_{15}Fe_5S_{25}$, the high pressure phase density does exceed the density calculated for the ambient pressure phase.

Acknowledgments

The authors gratefully acknowledge the research support provided by grants from the Robert A. Welch Foundation, Houston, Texas, the National Science Foundation, and the Air Force Office of Scientific Research. We thank Professor R. L. Collins, Department of Physics, University of Texas at Austin, for permitting us to use his Mössbauer equipment and for the many helpful discussions concerning the interpretation of the data.

References

1. H. Y. Hong and H. Steinfink, *J. Solid State Chem.* **5**, 93 (1972).
2. W. M. Reiff, I. E. Grey, A. Fan, Z. Eliezer, and H. Steinfink, *J. Solid State Chem.* **13**, 32 (1975).
3. J. G. Cosgrove and R. L. Collins, *Nucl. Instr. and Methods* **95**, No. 2, 269–274 (1971).
4. L. F. Bates, "Modern Magnetism," 4th ed., p. 134, Cambridge University Press, New York (1963).
5. "International Tables for X-ray Crystallography," Vol. III, Kynoch Press, Birmingham, England (1962).
6. I. E. Grey, H. Hong, and H. Steinfink, *Inorg. Chem.* **10**, 340 (1971).
7. Bronger, Von W., *Z. Anorg. Allg. Chem.* **359**, 225 (1968).
8. R. D. Shannon and C. T. Prewitt, *Acta. Crystallogr.* **B25**, 925 (1969).
9. I. Bernal, B. R. Davis, M. L. Good, and S. Chandra, *J. Coord. Chem.* **2**, 61 (1972).
10. C. B. Shoemaker, *Z. Krist.* **137**, 225 (1973).
11. W. B. Pearson, "The Crystal Chemistry and Physics of Metals and Alloys," Wiley-Interscience, New York (1972).
12. S. Geller, *Acta Crystallogr.* **8**, 15 (1955).
13. G. D. Brunton and H. Steinfink, *Inorg. Chem.* **10**, 2301 (1971).